



Oblique reflection of large internal solitary waves in a two-layer fluid

Nakayama, Keisuke

Kakinuma, Taro

Tsuji, Hidekazu

(Citation)

European Journal of Mechanics - B/Fluids, 74:81-91

(Issue Date)

2019-04

(Resource Type)

journal article

(Version)

Accepted Manuscript

(Rights)

© 2018 Elsevier Masson SAS.

This manuscript version is made available under the CC-BY-NC-ND 4.0 license

<http://creativecommons.org/licenses/by-nc-nd/4.0/>

(URL)

<https://hdl.handle.net/20.500.14094/90006059>



1 **Oblique reflection of large internal solitary waves in a two-layer fluid**

2 Keisuke Nakayama ^a, Taro Kakinuma ^b and Hidekazu Tsuji ^c

3 ^a Graduate School of Engineering, Kobe University, Rokkodai-cho 1-1, Nada-ku,

4 Kobe city, 657-8501, Japan

5 ^b Graduate School of Science and Engineering, Kagoshima University, Kagoshima, 890-0065, Japan

6 ^c Research Institute for Applied Mechanics, Kyushu University, 6-1 Fukuoka, 816-8580, Japan

7
8 ^aCorresponding author. E-mail: nakayama@phoenix.kobe-u.ac.jp

9 Tel: +81 78 803 6056

10 Postal address: Rokkodai-cho 1-1, Nada-ku, Kobe city, 657-8501, Japan

11
12 **Abstract**

13 The oblique reflection of an incident internal solitary wave is investigated using a fully-nonlinear
14 and strongly-dispersive internal wave model. The 3rd order theoretical solution for an internal
15 solitary wave in a two-layer system is used for the incident solitary wave. Two different incident
16 wave amplitude cases are investigated, in which nine and eleven different incident angles are used
17 for the small and large incident amplitude cases respectively. Under both amplitudes, at least for the
18 cases investigated here, relatively smaller incident angles result in Mach reflection while relatively
19 larger incident angles result in regular reflection. Under Mach-like reflection generation of a ‘stem’
20 is observed for a certain range of incident angles, in addition to the reflected wave. The stem is

found to have, in a certain sense, the characteristics of an internal solitary wave, though the maximum stem wave amplitude is less than four times as large as the original incident internal solitary wave. The stem length is confirmed to increase faster for the larger incident wave amplitude. The maximum amplification factor for the small incident wave is the same as in previous studies. However, the maximum amplification factor for the large incident wave is less than that for the small wave. The results of these calculations are compared with those of the corresponding KP theory and it is found that a lower amplification factor may be a significant characteristic of internal solitary waves.

Keywords: variational principle; solitary wave; interaction; Mach stem; two-layer system; KP theory

1. Introduction

The mechanism of occurrence of large amplitude surface waves in shallow water regions has been discussed [Kharif and Pelinovsky, 2003], along with similar kinds of problems related to “Freak waves” in deep water. Kharif and Pelinovsky [2003] suggested that one of the significant causals of “Freak waves” is soliton resonance, which occurs due to the interaction of two solitary waves. In contrast to surface waves, previous studies have revealed that large-amplitude internal solitary waves may exist in the ocean based on images taken from the aircraft and satellites [Wang and Pawlowicz, 2012] [Xue et al., 2013]. For instance, Helfrich and Melville [2006] provided images of the interaction of internal solitary waves. In a recent study, Shimizu and Nakayama [2017] provided the occurrence of large-amplitude internal solitary waves due to resonance in the Andaman Sea by using a three-dimensional MITgcm simulations [Marshall et al., 1997] [Adcroft et al., 1997]. Shimizu and Nakayama [2017] demonstrated that the theoretical and numerical studies are required to clarify how such a large-amplitude internal solitary wave occur. However, the interaction of internal solitary waves has not been adequately investigated in previous studies. For example, Yuan et al. [2018] demonstrated the importance of nonlinear interaction of soliton resonance of internal waves with the topographic effect. In particular, the study of internal solitary waves, as steady progressive nonlinear waves, should be a promising avenue for not only clarifying the phenomenon itself but also for understanding the behavior of nonlinear internal waves. Therefore, this study aims to investigate the two-dimensional interactions of internal solitary waves due to soliton resonance by using numerical simulation.

For surface waves, Miles [1977] theoretically proposed the concept of “resonance”, which is the interaction of three solitary waves with different incident angles in the two-dimensional weakly nonlinear interaction of shallow water solitary waves. Miles applied this concept to the phenomenon called Mach reflection in which the third solitary wave (stem), together with usual reflected wave, is generated around the wall during the reflection process. The theory insists that the stem amplitude is 4 times the amplitude of the incident solitary wave at the critical incident angle defined as the angle when the maximum amplitude occurs and the angle between Mach and regular reflection under weakly nonlinear condition [Melville, 1980]. Mach reflection occurs when an incident angle is less than the critical incident angle. Funakoshi [1980] numerically computed the reflection problem using the Boussinesq equations for shallow water in which an incident solitary wave propagating along one straight wall was reflected due to another straight wall oblique to the straight wall, roughly supporting Miles’ results under weakly nonlinear conditions (**Fig. 1**). However, regarding the maximum amplitude, it seems that the critical incident angle in Funakoshi’s result was somewhat smaller than that of Miles. For an incident angle sufficiently larger than the critical incident angle, Funakoshi’s result is in better agreement with the other result of Miles (perturbation solutions in weak interaction) [Miles 1977]. However, Tanaka [1993] investigated the oblique reflection of a large amplitude solitary wave by numerically solving the inviscid water wave equations using a spectral method, finding that the maximum amplitude is about three times the amplitude of the incident solitary wave. The critical incident angle in Tanaka’s numerical result was much smaller than the value predicted by Miles’ theory. Yeh et al. [2010] and Li et al. [2011] analytically and

experimentally studied the reflection of an obliquely incident solitary wave, finding that the maximum fourfold amplification predicted by Miles was not realized in a laboratory experiment under strong nonlinear condition. Gidel et al. [2017] also showed the slightly small amplification factor compared to Miles. These studies suggest that there are some differences between the weakly nonlinear theory of Miles and other numerical and experimental results. Though Kodama [2010] and Kodama et al. [2016] improve theoretical result by detailed analysis for the Kadomtsev-Petviashvili (KP) equation which is a horizontally two-dimensional version of the KdV equation, the reason for the quantitative differences of amplification in the neighborhood of the margin between regular and Mach reflection is still unclear. It has been suggested that fully-nonlinear and strongly-dispersive wave equations are needed for analyzing the deformations of solitary waves.

For internal waves, Maxworthy [1980] carried out laboratory experiments that showed the occurrence of a Mach stem in the interaction of two internal solitary waves. However, there are few experimental studies regarding the occurrence of a Mach stem in stratified flow fields. Theoretically, Tsuji and Oikawa [2007] demonstrated that the importance of “critical depth” which may suppress amplification rate due to soliton resonance by using the Extended Kadomtsev-Petviashvili equation. Critical depth is obtained from weakly nonlinear analysis for a two-layer system where internal solitary waves do not exist and corresponds to a conjugate flow [Lamb, 1998] [Tsuji and Oikawa, 2007] [Nakayama et al., 2012]. Oikawa and Tsuji [2006] showed that as the amplification of internal solitary waves in the region where two internal solitary waves propagate in different directions and cross each other decreases, the critical depth corresponds to the depth where a conjugate flow

appears. To analyze such a strongly nonlinear effect, higher order equations for internal waves are required. For example, Lamb [1998], Nakayama [2006] and Nakayama and Imberger [2010] demonstrated that a three-dimensional numerical model using a high-resolution mesh is useful for the deformation of internal solitary waves. However, the computational cost is too expensive to analyze the interaction of two internal solitary waves. Therefore, vertically integrated model may be applied to solve internal solitary wave interactions [Choi and Camassa, 1999] [Horn et al., 2000] [Horn et al., 2002]. For example, Choi and Camassa [1999] introduced higher order equations for internal waves, but it is needed to be extended to a horizontally two-dimensional system, such as a Kadomtsev-Petviashvili equation.

Nakayama and Kakinuma [2010] developed the Fully-nonlinear and strongly-Dispersive Internal wave equations in a 2 layer system (FDI-2s equations), which can be applied to a horizontally two-dimensional system without assuming a weak-nonlinearity along the perpendicular direction to the progress direction, such as a Kadomtsev-Petviashvili equation. Thus, we apply the FDI-2s equations to investigate the interaction of two internal solitary waves due to soliton resonance in a two-layer system. Firstly, we investigate the applicability of the FDI-2s equations for large amplitude internal solitary waves by comparing with laboratory experiments by Koop and Butler [1981]. Also, the FDI-2s equations are applied to reproduce deformation of internal waves by using laboratory experiments [Horn et al., 2001] [Horn et al., 2002]. Finally, we investigated the interaction of two internal solitary waves by giving the total 20 different conditions regarding an initial amplitude and an incident angle (**Fig. 1** and **Table 1**).

2. Methods

2.1 Fully-nonlinear and strongly-dispersive internal wave equations in a two-layer system

We consider waves propagating in a stable two-layer inviscid fluid at rest as shown in **Fig. 2** where two-layers are indicated as $i = 1$ and $i = 2$ from top to bottom. The flow is assumed to be incompressible. The depth and density of each layer is indicated by h_i and ρ_i , respectively, with $\rho_1 < \rho_2$. By assuming irrotational flow, the velocity potential ϕ_i is introduced as;

$$\mathbf{u}_i = \nabla \phi_i \quad \text{and} \quad w_i = \frac{\partial \phi_i}{\partial z}, \quad (1)$$

$$\nabla = \left(\frac{\partial}{\partial x}, \frac{\partial}{\partial y} \right), \quad (2)$$

where, \mathbf{u}_i is the horizontal velocity vector for the layer i , and w_i is the vertical velocity for the layer i .

The functional for the variational problem is obtained by adding terms for interfacial pressure into the variational method by Luke [1967] and disregarding vorticity terms

$$F_i[\phi_i, \zeta_{i,j}] = \int_{t_0}^{t_1} \iint_A \int_{\zeta_{i,0}}^{\zeta_{i,1}} \left\{ \frac{\partial \phi_i}{\partial t} + \frac{1}{2} (\nabla \phi_i)^2 + \frac{1}{2} \left(\frac{\partial \phi_i}{\partial z} \right)^2 + gz + \frac{p_{i-j} + P_i}{\rho_i} \right\} dz dA dt, \quad (3)$$

$$P_i = \sum_{k=1}^{i-1} (\rho_i - \rho_k) g h_k, \quad (4)$$

where g is the gravitational acceleration, A is the orthogonal projection of the volume occupied by the fluid onto the xy plane, and $\zeta_{i,1}$ and $\zeta_{i,0}$ are the interfacial displacement of the upper and lower interface for layer i .

In order to derive a set of two-dimensional horizontal equations, the velocity potential is expanded into the sum of $Z_{i,\alpha}$ multiplied by their weightings $f_{i,\alpha}$ by following Isobe [1995].

$$\phi_i(x, y, z, t) = \sum_{\alpha=0}^{N-1} Z_{i,\alpha}(z, h_i(x, y, t)) f_{i,\alpha}(x, y, t). \quad (5)$$

After substituting (5) into (3) and integrating (3) vertically, the Euler-Lagrange equations are obtained by applying the variational principle [Isobe, 1995]. For our study of internal waves, we assume the displacement of the water surface is zero which simplifies the model. Following Isobe [1995], the vertically distributed function, $Z_{i,\alpha}$, is determined by

$$Z_{i,\alpha} = z^\alpha. \quad (6)$$

Finally, the equations for fully-nonlinear and strongly-dispersive internal wave equations are:

[1-layer]

$$\zeta^\alpha \frac{\partial \zeta}{\partial t} + \frac{1}{\alpha + \beta + 1} \nabla \left(\zeta^{\alpha + \beta + 1} \nabla f_{1,\beta} \right) - \frac{\alpha \beta}{\alpha + \beta - 1} \zeta^{\alpha + \beta - 1} f_{1,\beta} = 0, \quad (7)$$

$$\zeta^\beta \frac{\partial f_{1,\beta}}{\partial t} + \frac{1}{2} \zeta^{\beta + \gamma} \nabla f_{1,\beta} \nabla f_{1,\gamma} + \frac{\beta \gamma}{2} \zeta^{\beta + \gamma - 2} f_{1,\beta} f_{1,\gamma} + g \zeta + \frac{p_1}{\rho_1} = 0, \quad (8)$$

[2-layer]

$$\zeta^\alpha \frac{\partial \zeta}{\partial t} + \frac{1}{\alpha + \beta + 1} \nabla \left\{ \left(\zeta^{\alpha + \beta + 1} - b^{\alpha + \beta + 1} \right) \nabla f_{2,\beta} \right\} - \frac{\alpha \beta}{\alpha + \beta - 1} \left(\zeta^{\alpha + \beta - 1} - b^{\alpha + \beta - 1} \right) f_{2,\beta} = 0, \quad (9)$$

$$\zeta^\beta \frac{\partial f_{2,\beta}}{\partial t} + \frac{1}{2} \zeta^{\beta + \gamma} \nabla f_{2,\beta} \nabla f_{2,\gamma} + \frac{\beta \gamma}{2} \zeta^{\beta + \gamma - 2} f_{2,\beta} f_{2,\gamma} + g \zeta + \frac{p_1 + (\rho_2 - \rho_1) g h_1}{\rho_1} = 0, \quad (10)$$

where, for α and β the summation convention is applied.

From now on, we call the Fully-nonlinear and strongly-Dispersive Internal wave equations (7) to (10), the FDI-2s equations. It should be noted that the FDI-2s can be extended to a multi-layer system based on the Euler-Lagrange equations, the Fully-nonlinear and strongly-Dispersive Internal wave equations in a multi-layer system (FDI-MLS equations) [Nakayama and Kakinuma, 2010].

2.2 The 3rd order theoretical solution for an internal solitary wave and performance evaluation

In the numerical simulations it was necessary to specify a large amplitude internal solitary wave, which progresses with little deformation, as an initial condition. When the KdV theoretical solution is used as an initial large amplitude internal solitary waves and the FDI-2s equations are used in the computation, small-amplitude high-frequency internal waves are likely to occur due to the adjustment of the initial approximate wave which results in a decrease in the amplitude of the internal solitary wave [Lamb, 2002] [Nakayama, 2006]. Therefore, as an initial condition we used a 3rd order theoretical solution for the internal solitary wave in a two-layer fluid, which was obtained by simplifying the 9th order solution of Mirie and Pennell [1989] (see APPENDIX A).

We investigated the characteristics of the 3rd order theoretical solutions and the FDI-2s equations for the analysis of internal solitary waves based on the laboratory experiments of Koop and Butler [1981], which showed the relationship between the amplitude, a_0 , and effective wavelength, λ_l , of internal solitary waves (**Fig. 3**). The amplitude and effective wavelength of the

FDI-2s equations were obtained by conducting numerical computations with the initial condition of the 3rd order theoretical solutions. We applied the two-layer shallow water configuration used by Koop and Butler which used $h_1 = 0.06948$ m, $h_2 = 0.01366$ m and $\rho_1 / \rho_2 = 0.63$. The mesh grid interval, $\Delta x = 0.004$ m, the time step, $\Delta t = 0.00005$ s were used in the numerical computations. The thin solid lines envelope the measurement plots by Koop and Butler [1981] for the laboratory experiments of $\rho_1 / \rho_2 = 0.63$ and $h_1 / h_2 = 5.09$. The 3rd order theoretical solutions are found to agree better with the laboratory results than the KdV theoretical solutions. The FDI-2s equations agree with the 3rd order theoretical solutions up to $a_0 / h_2 = 0.25$, and then λ_I / h_2 tends to be larger than the 3rd order theoretical solutions, which agrees with the fully-nonlinear solutions obtained using numerical computations by Grue *et al.* [1997] in FIGURE 5 of Choi and Camassa [1999].

In order to demonstrate the applicability of the FDI-2s equations for the deformation of internal solitary waves, the FDI-2s equations were applied to the laboratory experiment of Horn *et al.* [2000] [2002]. The length, width and height of their tilting tank were 6.0 m, 0.30 m and 0.29 m, respectively. For the laboratory experiment, $h_1 = 0.232$ m, $h_2 = 0.058$ m, $\rho_2 - \rho_1 = 20.0$ kg m⁻³, and a tilting angle = 0.5° were chosen (**Fig. 4(a)**). The interfacial thickness was less than 0.01 m, which provides a two-layer-like system. The total mechanical energy (kinetic + potential) due to a tilting density interface decreases during the deformation from the internal seiche to a train of internal solitary waves due to viscous losses [Horn *et al.*, 2000 and 2002]. Therefore, energy dissipation due to viscous losses at the interface and the boundaries was added to the FDI-2s equations. As a result, the interfacial displacement from the FDI-2s equations agrees very well with

Horn *et al.*'s laboratory experiment, thereby confirming the robustness of the FDI-2s equations for analyzing the excitation of internal solitary waves (**Fig. 4(b)**).

2.3 Boundary conditions

To analyze the two-dimensional interaction of internal solitary waves, we adopt a finite difference method for a type of domain used by Funakoshi [1980] (**Fig. 1**). It is necessary to resolve the zero momentum boundary condition for the oblique boundary condition in the computational domain (**Fig. 1**). Simanjuntak *et al.* [2009] introduced a numerical computation technique whereby zero normal velocity boundary conditions can be successfully applied to reproduce internal wave reflections in a stratified flow field by comparing with analytical solutions. Since a velocity potential is used in this study, it is not possible to directly apply the zero normal velocity boundary condition. Therefore, in this study we propose a new technique for zero normal velocity boundary conditions by following Simanjuntak *et al.* [2009]. The intersection point of the oblique boundary line and the perpendicular line to the oblique boundary from a node outside of the computational domain is defined as (x', y') (**Fig. 5**). The unknown velocity potential, $\phi_{i,j}$, is determined by applying the Galerkin method using the known velocity potentials, $\phi_{i-1,j}$, $\phi_{i,j+1}$ and $\phi_{i-1,j+1}$, so as to satisfy the zero normal velocity boundary conditions shown in (11) on the oblique boundary (see APPENDIX B).

$$\frac{\partial \phi'_{i,j}}{\partial \mathbf{n}} = 0. \quad (11)$$

3. Results

3.1 Computational conditions and critical incident angle of an internal solitary wave

Two different amplitudes of initial internal solitary waves A and B were used in the simulations. The common computational conditions of the numerical analysis were that the upper layer depth was 0.20 m, the lower layer depth was 0.80 m, and the ratio of the density between the upper and lower layers was 0.5 ($h_2 / h_1 = 4.00$), which is a similar set up to that of Koop and Butler [1981], ($\rho_1 / \rho_2 = 0.63$ and $h_1 / h_2 = 5.09$), though the depth of the layers is reversed. The small and large normalized amplitudes of the initial internal solitary waves, a_0 / h_2 , were 0.01 and 0.05, are 4 % and 20 % of the upper layer depth, respectively (**Fig. 6**). In the large 0.04 m ($a_0 / h_2 = 0.05$) amplitude case, the 3rd order internal solitary wave solution was confirmed to have wider wavelength compared to the KdV theory, which has been confirmed in a previous study [Nakayama, 2006] (also see **Fig. 3**).

To predict an amplification factor, the definition of parameter κ comes from Yeh *et al.* [2010] who modified Miles' result.

$$\kappa = \frac{\tan(\varphi)}{\sqrt{3p \frac{a_0}{h_2} \cos(\varphi)}} = \frac{\tan(\varphi)}{\tan(\varphi_c) \cos(\varphi)} \quad (12)$$

where a_0 is the amplitude of incident internal solitary wave (see APPENDIX C for details, including the definition of parameter, p , (C2)) and φ_c is the critical incident angle by Miles [1977].

Finally, the amplification factor, a_f , can be obtained as

$$a_f = \begin{cases} (1 + \kappa)^2 & \kappa < 1 \quad \text{Mach reflection} \\ \frac{4}{1 + \sqrt{1 - \kappa^{-2}}} & \kappa > 1 \quad \text{regular reflection} \end{cases} \quad (13)$$

where a_f is the ratio of the amplitude at the oblique boundary to the amplitude of the incident internal solitary wave.

The critical incident angle, φ_c , corresponds to the boundary between Mach and regular reflection.

According to Miles [1977], the ratio of the maximum amplitude to the amplitude of the incident internal solitary wave (we call this the maximum amplification factor) occurs when the angle of the incident internal solitary wave is equal to φ_c . As the critical incident angle obtained from the numerical computations, φ_c , is expected to be different from the modified Miles prediction, the critical incident angle obtained from the modified Miles prediction, φ_{c_kp} , is given by

$$\frac{\tan(\varphi_{c_kp})}{\cos(\varphi_{c_kp})} = \sqrt{3p \frac{a_0}{h_2}}. \quad (14)$$

In the small amplitude case, φ_{c_kp} obtained from (14) was 14.4 degrees, while it was 27.7 degrees for the large amplitude case. Therefore, for the small amplitude case, nine different incident angles were given corresponding to cases A1 to A9: 10, 11, 12, 12.5, 13, 14, 15, 20 and 30 degrees (**Table 1**). On the other hand, for the large amplitude case eleven different incident angles were given corresponding to cases B1 to B11: 10, 12, 14, 16, 18, 20, 23, 26, 28, 30 and 40 degrees (**Table**

1). Since the very small time step is required due to the use of the variational principle, linear theory shows that the celerity corresponds to the Courant-Friedrichs-Lewy condition, 0.00221. Although parallel computation was conducted using 12 CPUs using openMP, it took about 2500 s for the amplitude of a stem to reach the maximum amplitude in case A4, which was the most expensive runtime cost case, and it is necessary to prepare $7,200 \times 1,500 = 10,800,000$ meshes in the direction of progress, leading to a runtime cost that was too expensive. Therefore, we carried out actual computations only in the effective computational domains in order to reduce the runtime cost (**Fig. 7**). The left boundary of the effective computational domain had a sponge layer to reduce the internal wave energy, and perfect reflection conditions were specified at the top boundary in order to sustain the internal solitary wave energy during its progression. **Fig. 7** demonstrates that the stem was formed due to reflection from the oblique boundary.

3.2 Stem length and wave amplitude

Stem formation was investigated for all cases in order to clarify the influence of the incident angle on the development of the stem length (**Fig. 8**). Since φ_{c_kp} were 14.4 and 27.7 degrees for case A and case B, it was expected that a stem would be formed in cases A1 to A6 (incident angles between 10 and 14 degrees) and in cases B1 to B8 (incident angles between 10 and 26 degrees). A stem was formed in cases A1 to A6 and cases B1 to B8. However, the stem length reached a steady state in cases A5, A6, B7 and B8, although the stem length should keep increasing if the stem is due

to Mach reflection. Therefore, the crests in cases A5, A6, B7 and B8 are considered to occur due to regular reflection. In contrast, the cases from A1 to A4 and cases from B1 to B6 are considered to have a ‘stem’ due to Mach reflection because the stem length increased linearly in time.

Previous studies have found that the larger the amplitude of an incident internal solitary wave, the faster the stem extends, which was investigated here by comparison of the same incident angle between cases A1 and B1, and cases A3 and B2. The extension speed of a stem under case B1 with an incident angle of 10 degrees was 2.52 times as fast as under case A1 when $t / (h_2 / c_0) = 553$. The stem extension speed under case B2 was 2.91 times as fast as under case A3 for an incident angle of 12 degrees over $t / (h_2 / c_0) = 553$. Therefore, we confirmed that the stem extension speed increases with increasing amplitude of the incident internal solitary wave when other conditions are the same.

The time taken to reach the maximum amplitude due to the internal solitary wave interaction was plotted against each incident angle of the internal solitary wave (**Fig. 9**). The duration for the large amplitude case was shorter than the small amplitude case. The maximum duration for each small and large amplitude case appeared in case A4 and B6 when φ_c was less than φ_{c_kp} shown in (14). Interestingly, when a stem exists, cases A4 and B6 correspond to the maximum incident angle cases, and the smaller the incident angle, the faster the stem extension speed. In contrast, when incident angles are closer to φ_c , amplification factors and durations become larger and longer until the stem reaches a stationary state. Therefore, cases A4 and B6 took the longest to reach the maximum amplitude for the small and large amplitude cases, respectively.

The amplification factor obtained from numerical simulations were investigated using the KP theory ((14) and **Fig. 10**). The small amplitude case showed a maximum amplification factor of about 3.4, which agrees with previous studies [Funakoshi, 1980] and is smaller than the maximum value (= 4.0). For the large amplitude case the maximum amplification was found to be about 3.0, which is similar to previous studies [Tanaka, 1993] [Yeh et al., 2010] related to the interaction of large amplitude surface solitary waves. For smaller incident angles the amplification factor agrees well with the predictions of KP theory (**Fig. 10**). Interestingly, cases A5, A6, B7 and B8, in which the crest reaches steady state, are found to be located between the maximum amplification factor case and φ_{c_kp} , which is categorized as a regular reflection. From **Figs. 8-10**, it can be seen that the maximum amplification occurred when the incident angles were less than φ_{c_kp} (cases A4 and B6) and when the time taken to reach the maximum amplitude was longest for the small and large amplitude cases, respectively.

4. Discussion

4.1 Limiting wave amplitude of soliton resonance

Li *et al.* [2011] and Tanaka [1993] found from experimental and numerical results for surface waves that amplification was suppressed when the amplitude of an initial surface wave was relatively large, which corresponds to a large φ_{c_kp} . In particular, when the amplitude of an incident surface wave is large, the maximum amplification factor has been found to be less than 3.0, based on

numerical computations by Tanaka [1993]. Therefore, although this suppression close to ϕ_{c_kp} has been seen in surface waves in previous studies, the effect of large amplitudes may also be inherent to internal waves.

There may be another possible explanation for the suppression of amplification. Weakly nonlinear analysis for a two-layer system yields a critical depth where internal solitary waves do not exist because the nonlinearity vanishes and dispersion prevails [Lamb, 1998] [Tsuji and Oikawa, 2007] [Nakayama et al., 2012]. Therefore, in a two-layer system, the critical depth from the water surface is given by (15).

$$h_c = h_1 + a_c = \frac{\sqrt{\rho_1}(h_1 + h_2)}{\sqrt{\rho_1} + \sqrt{\rho_2}}. \quad (15)$$

where h_c is the critical depth from the water surface, and a_c is the maximum possible wave amplitude.

Tsuji and Oikawa [2007] demonstrated that resonance is suppressed when the initial density interfacial level is close to the critical depth by using the Extended Kadomtsev-Petviashvili equation. If the height of the stem of resonance is equal to the distance between the critical depth and the interface at rest, the corresponding amplification factors are 26.75 and 5.35 for the small and large amplitude cases, respectively. Therefore, since the density interface of the amplified internal solitary wave was closer to the critical depth for the large amplitude case compared to the small amplitude

case, the amplification due to resonance of two internal solitary waves may be suppressed for the large amplitude case.

4.2 Characteristics of stem

In previous studies, the stem induced by resonance was investigated by assuming that the stem is an internal solitary wave. To confirm whether the stem is an internal solitary wave or not, the shape of the stem was compared to the 3rd order theoretical solutions (**Fig. 11**). The largest amplitude case, case B6, was selected and compared to the 3rd order theoretical solutions, showing very good agreement with slightly larger effective wavelength of the FDI-2s equations, which shows the same tendency when a_0 / h_2 is about 0.6 in **Fig. 3**. The normalized celerity by linear theory was 1.573 while the celerity of the incident internal solitary wave was 1.356. Therefore, a stem has the potential to be an internal solitary wave from the perspective of the shape of the density interface. If a stem is an internal solitary wave, it progresses without having any decay or deformation. We thus made an attempt to carry out one-dimensional numerical computations using the FDI-2s equations specifying the shape of the density interface displacement and the velocity potential of the stem from cases A1, A5, B1 and B6 (**Fig. 12**). For case B6 there was a slight decrease in amplitude due to the formation of high-frequency internal waves, which follow the stem. However, the decrease in amplitude was negligible, and all cases kept the shape of the original stem and waves propagated

with speeds of an internal solitary wave, which demonstrates that stems induced by the resonance of internal solitary waves have the characteristics of an internal solitary wave.

5. Conclusion

The oblique reflection of an internal solitary wave in a two-layer system has been studied using the FDI-2s equations. For the small amplitude case: $a_0 / h_2 = 0.01$, the maximum amplification factor was found to be about 3.4. The amplification factor followed (14) in the region where a Mach stem occurred and the amplification factor was less than the Miles prediction, 4. The critical incident angle obtained from the numerical computations was confirmed to be equal to the critical incident angle obtained from the modified Miles prediction, φ_{c_kp} . The maximum amplification factor reached about 3.0 when the amplitude of the initial internal solitary wave was large (large amplitude case: $a_0 / h_2 = 0.05$). It may thus be expected that the larger φ_{c_kp} is, the smaller the amplification factor, which is expected based on the experimental and numerical results by Li *et al.* [2011] and Tanaka [1993] for surface waves. However, there is the possibility that a maximum possible wave amplitude exists when the density interfacial level is close to the critical depth.

6. Author contribution

K. Nakayama designed the all numerical computations and wrote most of the paper and performed theoretical analysis. T. Kakinuma and H. Tsuji discussed about the numerical

computational results with K. Nakayama. All authors read and commented on drafts of this paper.

Acknowledgments

We wish to thank Emeritus Professor Masayuki Oikawa for constructive comments, and an anonymous reviewer for their constructive comments, which have contributed to a significant improvement in the manuscript. This work was supported by the Japan Society for the Promotion of Science under grant 18H01545. This work was also supported in part by the Collaborative Research Program of Research Institute for Applied Mechanics, Kyushu University, and Research Center for Urban Safety and Security, Kobe University.

358 **APPENDIX A**

359 The 3rd order equations for an internal solitary wave are obtained by using the 9th order internal
 360 solitary wave equations [Mirie and Pennell, 1989].

361
$$h = -h_1 + \zeta \tag{A1}$$

362
$$\zeta / h_2 = \varepsilon A_{11} S + \varepsilon^2 (A_{21} S + A_{22} S^2) + \varepsilon^3 (A_{31} S + A_{32} S^2 + A_{33} S^3) \tag{A2}$$

363
$$S = \text{sech}^2 X \tag{A3}$$

364
$$X = \frac{\sqrt{3K\varepsilon}}{2h_2} (x - x_0 - C_R t) \tag{A4}$$

365
$$C_R = \sqrt{gh_0} C_0 (1 + \varepsilon C_1 + \varepsilon^2 C_2 + \varepsilon^3 C_3) \tag{A5}$$

366
$$C_0 = \sqrt{\frac{1 - \sigma}{1 + \sigma / \gamma}} \tag{A6}$$

367
$$\varepsilon = a_0 / h_2 \tag{A7}$$

368
$$A_{11} = \begin{cases} 1 & \sigma < \gamma^2 \\ -1 & \sigma > \gamma^2 \end{cases} \tag{A8}$$

369
$$A_{21} = \frac{1}{K(1 + \sigma\gamma)} \left[-\frac{1}{2} K^2 A_{11} (1 + \sigma\gamma^3) - K(1 - \sigma) + 2A_{11} (1 + \sigma / \gamma^3) \right] \tag{A9}$$

370
$$A_{22} = \frac{1}{2K(1 + \sigma\gamma)} \left[\frac{3}{2} K^2 A_{11} (1 + \sigma\gamma^3) + 2K(1 - \sigma) - 2A_{11} (1 + \sigma / \gamma^3) \right] \tag{A10}$$

371
$$A_{31} = \frac{1}{K(1 + \sigma\gamma)} \left[-\frac{K^2}{5} (1 - \sigma\gamma^2) + \frac{2}{3} K A_{11} (1 + \sigma / \gamma) - \frac{8}{3} (1 - \sigma / \gamma^4) - K A_{21} A_{11} (1 - \sigma) + 4A_{21} (1 + \sigma / \gamma^3) \right]$$

$$\begin{aligned}
& -2KA_{21}C_1(1+\sigma\gamma) - \frac{K^2}{30}A_{22}(1+\sigma\gamma^3) - \frac{2}{3}KA_{22}A_{11}(1-\sigma) + 2A_{22}(1+\sigma/\gamma^3) - KA_{22}C_1(1+\sigma\gamma) \\
& + \frac{4}{3}A_{22}C_2(1+\sigma/\gamma) - K^2A_{11}C_1(1+\sigma\gamma^3) - 2KC_1(1-\sigma) + 4A_{11}C_1(1+\sigma/\gamma^3) \Big] \quad (A11)
\end{aligned}$$

$$\begin{aligned}
& A_{32} = \frac{1}{K(1+\sigma\gamma)} \left[\frac{3}{5}K^3A_{11}(1+\sigma\gamma^5) - \frac{K^2}{5}(1-\sigma\gamma^2) - \frac{K}{3}A_{11}(1+\sigma/\gamma) + \frac{3}{4}K^2A_{21}(1+\sigma\gamma^3) + 2KA_{21}A_{11}(1-\sigma) \right. \\
& - 3A_{21}(1+\sigma/\gamma^3) - \frac{21}{20}K^2A_{22}(1+\sigma\gamma^3) + \frac{K}{3}A_{22}A_{11}(1-\sigma) - A_{22}(1+\sigma/\gamma^3) + \frac{3}{2}K^2A_{11}C_1(1+\sigma\gamma^3) + 2KC_1(1-\sigma) \\
& \left. - 2A_{11}C_1(1+\sigma/\gamma^3) - 2KA_{22}C_1(1+\sigma\gamma) + \frac{4}{3}(1-\sigma/\gamma^4) \right] \quad (A12)
\end{aligned}$$

$$\begin{aligned}
& A_{33} = \frac{1}{K(1+\sigma\gamma)} \left[-\frac{3}{5}K^3A_{11}(1+\sigma\gamma^5) + \frac{9}{20}K^2(1-\sigma\gamma^2) - \frac{K}{3}A_{11}(1+\sigma/\gamma) + \frac{1}{3}(1-\sigma/\gamma^4) + \frac{31}{20}K^2A_{22}(1+\sigma\gamma^3) \right. \\
& \left. + \frac{4}{3}KA_{22}A_{11}(1-\sigma) - A_{22}(1+\sigma/\gamma^3) \right] \quad (A13)
\end{aligned}$$

$$K = \frac{1-\sigma/\gamma^2}{1+\sigma\gamma} A_{11} \quad (A14)$$

$$C_1 = \frac{1-\sigma/\gamma^2}{2(1+\sigma/\gamma)} A_{11} \quad (A15)$$

$$C_2 = \frac{1}{2(1+\sigma/\gamma)} \left[\frac{K^2}{5}(1+\sigma\gamma^3) + 3(1+\sigma/\gamma)C_1^2 \right] \quad (A16)$$

$$\begin{aligned}
& C_3 = \frac{1}{2(1+\sigma/\gamma)} \left[\frac{2}{35}K^3(1+\sigma\gamma^5) + \left(\frac{K^2}{5}A_{21}A_{11} + \frac{2K^2}{5}C_1 \right) (1+\sigma\gamma^3) + (2KA_{21}A_{11}C_1 + KC_1^2 + 2KC_2) \right. \\
& \left. (1+\sigma\gamma) - (A_{21}A_{11}C_1^2 + 2A_{21}A_{11}C_2 + 2C_1C_2) (1+\sigma/\gamma) \right] \quad (A17)
\end{aligned}$$

where, a_0 is the amplitude of incident internal wave.

386 APPENDIX B

387 Velocity potential inside of a mesh is given by (B1) using the Galerkin method.

$$\begin{aligned}
 388 \quad \phi &= \phi_{i-1,j} \frac{x-x_{i-1,j}}{\Delta x} \frac{y-y_{i-1,j}}{\Delta y} + \phi_{i,j} \frac{x_{i,j}-x}{\Delta x} \frac{y-y_{i,j}}{\Delta y} \\
 389 \quad &+ \phi_{i-1,j+1} \frac{x-x_{i-1,j+1}}{\Delta x} \frac{y_{i-1,j+1}-y}{\Delta y} + \phi_{i,j+1} \frac{x_{i,j+1}-x}{\Delta x} \frac{y_{i,j+1}-y}{\Delta y} . \quad (B1)
 \end{aligned}$$

390 Zero normal velocity boundary condition is given as (B2).

$$391 \quad \frac{\partial \phi'_{i,j}}{\partial \mathbf{n}} = \frac{\partial x}{\partial \mathbf{n}} \frac{\partial \phi'_{i,j}}{\partial x} + \frac{\partial y}{\partial \mathbf{n}} \frac{\partial \phi'_{i,j}}{\partial y} = 0, \quad (B2)$$

$$392 \quad \frac{\partial \phi'_{i,j}}{\partial x} = \phi_{i-1,j} \frac{1}{\Delta x} \frac{y'-y_{i-1,j}}{\Delta y} - \phi_{i,j} \frac{1}{\Delta x} \frac{y'-y_{i,j}}{\Delta y} + \phi_{i-1,j+1} \frac{1}{\Delta x} \frac{y_{i-1,j+1}-y'}{\Delta y} - \phi_{i,j+1} \frac{1}{\Delta x} \frac{y_{i,j+1}-y'}{\Delta y}, \quad (B3)$$

$$393 \quad \frac{\partial \phi'_{i,j}}{\partial y} = \phi_{i-1,j} \frac{x'-x_{i-1,j}}{\Delta x} \frac{1}{\Delta y} + \phi_{i,j} \frac{x_{i,j}-x'}{\Delta x} \frac{1}{\Delta y} - \phi_{i-1,j+1} \frac{x'-x_{i-1,j+1}}{\Delta x} \frac{1}{\Delta y} - \phi_{i,j+1} \frac{x_{i,j+1}-x'}{\Delta x} \frac{1}{\Delta y}. \quad (B4)$$

394 Therefore, zero normal velocity boundary condition (B2) is rewritten as (B5).

$$\begin{aligned}
 395 \quad \frac{\partial \phi'_{i,j}}{\partial \mathbf{n}} &= \frac{\partial x}{\partial \mathbf{n}} \left[\phi_{i-1,j} \frac{1}{\Delta x} \frac{y'-y_{i-1,j}}{\Delta y} - \phi_{i,j} \frac{1}{\Delta x} \frac{y'-y_{i,j}}{\Delta y} + \phi_{i-1,j+1} \frac{1}{\Delta x} \frac{y_{i-1,j+1}-y'}{\Delta y} - \phi_{i,j+1} \frac{1}{\Delta x} \frac{y_{i,j+1}-y'}{\Delta y} \right] \\
 396 \quad &+ \frac{\partial y}{\partial \mathbf{n}} \left[\phi_{i-1,j} \frac{x'-x_{i-1,j}}{\Delta x} \frac{1}{\Delta y} + \phi_{i,j} \frac{x_{i,j}-x'}{\Delta x} \frac{1}{\Delta y} - \phi_{i-1,j+1} \frac{x'-x_{i-1,j+1}}{\Delta x} \frac{1}{\Delta y} - \phi_{i,j+1} \frac{x_{i,j+1}-x'}{\Delta x} \frac{1}{\Delta y} \right] = 0. \quad (B5)
 \end{aligned}$$

397 Finally, the unknown velocity potential, $\phi_{i,j}$, is determined from the known velocity potentials,

398 $\phi_{i-1,j}$, $\phi_{i,j+1}$ and $\phi_{i-1,j+1}$.

$$\begin{aligned}
 399 \quad \phi_{i,j} &= \left\{ \phi_{i-1,j} \left[(y'-y_{i-1,j}) \frac{\partial x}{\partial \mathbf{n}} + (x'-x_{i-1,j}) \frac{\partial y}{\partial \mathbf{n}} \right] + \phi_{i-1,j+1} \left[(y_{i-1,j+1}-y') \frac{\partial x}{\partial \mathbf{n}} - (x'-x_{i-1,j+1}) \frac{\partial y}{\partial \mathbf{n}} \right] \right. \\
 400 \quad &\left. - \phi_{i,j+1} \left[(y_{i,j+1}-y') \frac{\partial x}{\partial \mathbf{n}} + (x_{i,j+1}-x') \frac{\partial y}{\partial \mathbf{n}} \right] \right\} / \left[(y'-y_{i,j}) \frac{\partial x}{\partial \mathbf{n}} - (x'-x_{i,j}) \frac{\partial y}{\partial \mathbf{n}} \right]. \quad (B6)
 \end{aligned}$$

401

402

403 APPENDIX C

404 Here we describe the results of the KP equation and their modification for comparison to our
 405 numerical results for internal waves in a two-layer fluid system with a rigid lid shown in **Fig. 2**. It is
 406 also assumed that the interface is not near the critical depth. Details of derivation of the equations are
 407 omitted and only the results are described.

408 The KdV equation for waves propagating in the direction $\mathbf{n} = (\cos \varphi, \sin \varphi)$ in this system is
 409 written in the physical coordinates as

$$410 \quad \frac{\partial \zeta}{\partial t} + V \frac{\partial \zeta}{\partial \chi} - \frac{3Vp}{2h_2} \zeta \frac{\partial \zeta}{\partial \chi} + \frac{Vh_2^2 q}{6} \frac{\partial^3 \zeta}{\partial \chi^3} = 0 \quad (C1)$$

411 where, ζ is the displacement of the interface, $\chi = \mathbf{n} \cdot \mathbf{x} = x \cos \varphi + y \sin \varphi$ ($\mathbf{x} = (x, y)$ the position
 412 vector in a horizontal plane), t the time. The constants p and q are given by

$$413 \quad p = \frac{\sigma - \gamma^2}{\gamma(\gamma + \sigma)} \quad (C2)$$

$$414 \quad q = \frac{\gamma(1 + \gamma\sigma)}{\gamma + \sigma} \quad (C3)$$

$$415 \quad \gamma = \frac{h_1}{h_2} \quad (C4)$$

$$416 \quad \sigma = \frac{\rho_1}{\rho_2} \quad (C5)$$

417 The solitary wave solution of the KdV equation (C1) is given by

$$418 \quad \zeta = -a_0 \operatorname{sech}^2 \left\{ \sqrt{\frac{3pa_0}{4qh_2^3}} \left[\chi - \left(1 + \frac{pa_0}{2h_2} \right) Vt - \chi_0 \right] \right\} \quad (C6)$$

$$419 \quad V = \sqrt{gh_2 \gamma \frac{1 - \sigma}{\gamma + \sigma}} \quad (C7)$$

420 where, χ_0 is an arbitrary constant and we consider the case $p > 0$.

421 The KP equation for waves propagating almost in the x direction is in the physical
422 coordinates

$$423 \quad \frac{\partial}{\partial x} \left(\frac{\partial \zeta}{\partial t} + V \frac{\partial \zeta}{\partial x} - \frac{3Vp}{2h^2} \zeta \frac{\partial \zeta}{\partial x} + \frac{Vq}{6} h^2 \frac{\partial^3 \zeta}{\partial x^3} \right) + \frac{V}{2} \frac{\partial^2 \zeta}{\partial y^2} = 0 \quad (C8)$$

424 The solitary wave solution to this equation is

$$425 \quad \zeta = -a_1 \text{sech}^2 \left\{ \sqrt{\frac{3pa_1}{4qh_2^3}} \left[x + y \tan \varphi - V \left(1 + \frac{pa_1}{2h_2} + \frac{1}{2} \tan^2 \varphi \right) t - x_0 \right] \right\} \quad (C9)$$

426 where a_1 is an amplitude and x_0 is an arbitrary constant.

427 Now, transformation of the variables yields

$$428 \quad u = \frac{3p}{2h_2} \zeta \quad (C10)$$

$$429 \quad X = \frac{x - Vt}{\sqrt{qh_2}} \quad (C11)$$

$$430 \quad Y = \frac{y}{\sqrt{qh_2}} \quad (C12)$$

$$431 \quad T = \frac{2Vt}{3\sqrt{qh_2}} \quad (C13)$$

432 The KP equation (C8) is written as

$$433 \quad \frac{\partial}{\partial x} \left(4 \frac{\partial u}{\partial T} - 6u \frac{\partial u}{\partial X} + \frac{\partial^3 u}{\partial X^3} \right) + 3 \frac{\partial^2 u}{\partial Y^2} = 0 \quad (C14)$$

434 As the incident angle decreases in the KP equation, the oblique reflection of the solitary wave
435 due to a rigid wall changes from a regular type to a Mach type at the critical angle. The asymptotic
436 value of the factor of the maximum wave amplitude at the wall to the amplitude of the incident
437 solitary wave approaches four at the critical incident angle. For the KP equation (C14), it is known

438 that the amplification factor [29] can be given by

$$439 \quad \text{amplification factor} = \begin{cases} (1+\kappa)^2 & \kappa < 1 \\ \frac{4}{1+\sqrt{1-\kappa^{-2}}} & \kappa > 1 \end{cases} \quad (C15)$$

$$440 \quad \kappa = \frac{\tan(\varphi)}{\sqrt{3p \frac{a_0}{h_2}}} = \frac{\tan(\varphi)}{\tan(\varphi_c)} \quad (C16)$$

441 For shallow water waves, the equations corresponding to (C14) and (C15) may be called the
 442 Miles' prediction. The Miles' prediction does not agree with the numerical computations of
 443 Funakoshi [1980] and Tanaka [1993], or the experiments of Li *et al.* [2011]. However, Yeh, Li, and
 444 Kodama [2010] [2016] considered an explanation as follows: the KP equation is derived under the
 445 assumption of quasi-two-dimensionality, in which $\alpha = O(\epsilon^{1/2})$ and $\epsilon = O(a_0/h_2) \ll 1$. The solution
 446 (C9) of the KP equation (C8) is rewritten as follows by the use of χ :

$$447 \quad \zeta = -a_1 \text{sech}^2 \left\{ \sqrt{\frac{3pa_1}{4qh_2^3 \cos^2 \varphi}} \left[\chi - V \cos \varphi \left(1 + \frac{pa_1}{2h_2} + \frac{1}{2} \tan^2 \varphi \right) t - \chi_0 \right] \right\} \quad (C17)$$

448 If $\alpha = O(\epsilon^{1/2})$, $\cos \alpha = 1 - (1/2) \tan^2 \varphi + O(\epsilon^2)$ and the velocity of the above solitary wave
 449 solution becomes

$$450 \quad V \cos \varphi \left(1 + \frac{pa_1}{2h_2} + \frac{1}{2} \tan^2 \varphi \right) = V \left(1 + \frac{pa_1}{2h_2} + O(\epsilon^2) \right) \quad (C18)$$

451 Thus, if we define (C19), the solution (C17) approximates to the KdV solution as (C20)

$$452 \quad a_0 = \frac{a_1}{\cos^2 \varphi} = a_1 \left(1 + \tan^2 \varphi \right) = a_1 \left(1 + O(\epsilon) \right) \quad (C19)$$

$$453 \quad \zeta = -a_0 \text{sech}^2 \left\{ \sqrt{\frac{3pa_0}{4qh_2^3}} \left[\chi - V \left(1 + \frac{pa_0}{2h_2} \right) t - \chi_0 \right] \right\} + O(\epsilon) \quad (C20)$$

454 Therefore, the simulations and experiments should be compared with the Miles' prediction
455 (C15) with

456
$$\kappa = \frac{\tan(\varphi)}{\sqrt{3p \frac{a_0}{h_2} \cos \varphi}} \quad (C21)$$

457 Let us call the Miles' prediction (C15) with (C21) as the modified Miles' prediction. The
458 modified Miles' prediction for the shallow water waves agrees well with the numerical computations
459 and experiments except near the critical incident angle.

460

461

References

- [1] C. Kharif and E. Pelinovsky , Physical mechanisms of the rogue wave phenomenon, Euro. J. Mech. B/Fluids, 22 (2003) 603-634.
- [2] C. Wang and R. Pawlowicz, Oblique wave-wave interactions of nonlinear near surface internal waves in the Strait of Georgia, J. Geophys. Res. Oceans, 117 (2012) C06031.
- [3] J. Xue, H. C. Graber, B. Lund and R. Romeister, Satellite observation of a zipper-like internal waves-wave interaction pattern in the mid-Atlantic Bight, Int. Geosci. Remote Se. (2013) 1571-1574.
- [4] K. R. Helfrich and W. K. Melville, Long nonlinear internal waves, Annu. Rev. Fluid Mech. 38 (2006) 395-425.
- [5] K. Shimizu and K. Nakayama, Effects of topography and earth's rotation on the oblique interaction of internal solitary-like waves in the Andaman Sea, J. Geophys. Res., 122 (2017) 7449-7465.
- [6] C. Yuan, R. Grimshaw, E. Johnson and Z. Wang, Topographic effect on oblique internal wave-wave interactions, J. Fluid Mech. 856 (2018) 36-60.
- [7] J. Marshall, A. Adcroft, C. Hill, L. Perelman and C. Heisey, A finite-volume, incompressible Navier-Stokes model for studies of the ocean on parallel computers, J. Geophys. Res., 102 (1997) 5753-5766.
- [8] A. Adcroft, C. Hill and J. Marshall, Representation of topography by shaved cells in a height coordinate ocean model, Mon. Weather Rev., 125 (1997) 2293-2315.

- 482 [9] J. W. Miles, Resonantly interacting solitary waves, J. Fluid Mech. 79 (1977) 171-179.
- 483 [10] W. K. Melville, On the Mach reflection of a solitary wave, J. Fluid Mech. 98 (1980) 285-297.
- 484 [11] M. Funakoshi, Reflection of obliquely incident solitary waves, J. Phys. Soc. Jpn. 49 (1980)
- 485 2371-2379.
- 486 [12] J.W. Miles, Obliquely interacting solitary waves , J. Fluid Mech. 79 (1977) 157-169.
- 487 [13] M. Tanaka, Mach reflection of a large-amplitude solitary wave, J. Fluid Mech. 248 (1993)
- 488 637-661.
- 489 [14] H. Yeh, W. Li and Y. Kodama, Mach reflection and KP solitons in shallow water, Eur. Phys. J.
- 490 Special Topics 185 (2010) 97-111.
- 491 [15] W. Li, H. Yeh and Y. Kodama, On the Mach reflection of a solitary wave: revisited, J. Fluid
- 492 Mech. 672 (2011) 326-357.
- 493 [16] F. Gidel, O. Bokhove and A. Kalogirou, Variational modelling of extreme waves through
- 494 oblique interaction of solitary waves: application to Mach reflection, Nonlin. Processes
- 495 Geophys. 24 (2017) 43-60.
- 496 [17] Y. Kodama, KP solitons in shallow water, J. Phys. A: Math. Theor. 43, 434004 (2010) 1-54.
- 497 [18] Y. Kodama and H. Yeh, The KP theory and Mech reflection, J. Fluid Mech. 800 (2016)
- 498 766-786.
- 499 [19] T. Maxworthy, On the formation of nonlinear internal waves from the gravitational collapse of
- 500 mixed regions in two and three dimensions, J. Fluid Mech. 96 (1980) 47-64.

- 501 [20] H. Tsuji and M. Oikawa, Oblique interaction of solitons in an extended
502 Kadomtsev-Petviashvili equation, J. Phys. Soc. Jpn. 76 (2007) 84401-84408.
- 503 [21] K. G. Lamb and B. Wan, Conjugate flows and flat solitary waves for a continuously stratified
504 fluid, Phys. Fluids 10 (1998) 2061-2079.
- 505 [22] K. Nakayama, T. Shintani, K. Kokubo, Y. Maruya, T. Kakinuma, K. Komai and T. Okada,
506 Residual current over a uniform slope due to breaking of internal waves in a two-layer system,
507 J. Geophys. Res. 117 (2012) C10002.
- 508 [23] M. Oikawa and H. Tsuji, Oblique interactions of weakly nonlinear long waves in dispersive
509 systems, Fluid Dyn. Res. 38 (2006) 868-898.
- 510 [24] K. Nakayama, Comparisons of using CIP, compact and CIP-CSL2 schemes for internal solitary
511 waves, Int. J. Num. Method. Fluids, 51 (2006) 197-219.
- 512 [25] K. Nakayama and J. Imberger, Residual circulation due to internal waves shoaling on a slope,
513 Limnol. Oceanogr. 55 (2010) 1009-1023.
- 514 [26] W. Choi and R. Camassa, Fully nonlinear internal waves in a two-fluid system, J. Fluid Mech.
515 396 (1999) 1-36.
- 516 [27] D. A. Horn, L. G. Redekopp, J. Imberger and G. N. Ivey, Internal wave evolution in a
517 space-time varying field, J. Fluid Mech. 424 (2000) 279-301.
- 518 [28] D. A. Horn, J. Imberger, G. N. Ivey and L. G. Redekopp, A weakly nonlinear model of long
519 internal waves in closed basins, J. Fluid Mech. 467 (2002) 269-287.

- [29] K. Nakayama and T. Kakinuma, Internal waves in a two-layer system using fully nonlinear internal-wave equations, *Int. J. Num. Method. Fluids* 62 (2010) 574-590.
- [30] C. G. Koop and G. Butler, An investigation of internal solitary waves in a two-fluid system, *J. Fluid Mech.* 112 (1981) 225–251.
- [31] D. A. Horn, J. Imberger and G. N. Ivey, The degeneration of large-scale interfacial gravity waves in lakes, *J. Fluid Mech.* 434 (2001) 181-207.
- [32] J. C. Luke, A variational principle for a fluid with a free surface, *J. Fluid Mech.* 27 (1967) 395-397,.
- [33] M. Isobe, Time-dependent mild-slope equations for random waves, *Proc. of the 24th Int. Conf. on Coastal Eng., ASCE* (1995) 285-299.
- [34] K. G. Lamb, A numerical investigation of solitary internal waves with trapped cores formed via shoaling, *J. Fluid Mech.* 451 (2002) 109-144.
- [35] R. M. Mirie and S.A. Pennell, Internal solitary waves in a two-fluid system, *Phys. Fluids A* 1(6) (1989) 986-991.
- [36] J. Grue, H. A. Friis, E. Palm and P. O. Rusas, A method for computing unsteady fully nonlinear interfacial waves, *J. Fluid Mech.* 351 (1997) 223-252.
- [37] M. A. Simanjuntak, J. Imberger and K. Nakayama, Numerical wave drag due to stair-step topography in a geophysical flow model, *J. Geophys. Res.*, 114 (2009) C12020.

Figure captions

Fig. 1. Schematic horizontal plane view of a computation corresponding to the occurrence of Mach and regular reflection of a soliton with an incident angle of φ . θ indicates the reflection angle.

Fig. 2. Schematic diagram of a two-layer system. Upper and lower boundaries are considered as rigid walls.

Fig. 3 Comparisons with the laboratory experiments by Koop and Butler [22]. Thin solid lines indicate the region of the experiments' plots. Dashed and thick solid lines indicate the KdV theoretical solutions and the 3rd order theoretical solutions, respectively. Circles indicate numerical computation results by using the FDI-2s equations.

Fig. 4 Comparisons with the laboratory experiments by Horn *et al.* [17] [46] [47]. (a) Initial set up. (b) Comparisons of interfacial displacement at the Wavegauge B between the laboratory experiments and the FDI-2s equations.

Fig. 5. Schematic diagram for satisfying boundary conditions of momentum. Normal velocity to an oblique boundary should be zero.

Fig. 6. Initial waves. The solid lines shows the 3rd order theoretical solution and dashed line shows the KdV solution. (a) case A. (b) case B.

Fig. 7. Interfacial displacement of case B5. Each solid line square in the bottom figure indicates the computational region at the times indicated. Top three figures show enlarged progress of internal solitary wave at $t / (h_2 / c_0) = 0, 277$ and 498 .

Fig. 8. Time series of the length of a stem for case A and case B. Length is normalized by the lower layer depth. (a) cases A1 to A6. (b) cases B1 to B8.

Fig. 9. Time taken to reach the maximum amplitude due to the internal soliton resonance for small amplitude case (circles) and large amplitude case (stars).

Fig. 10. Comparisons with (13). Circles and stars denote case A and B from the FDI-2s equations. (a) Normalized amplification factor vs κ for case A and B. Solid lines show (13) [27] [30] [31]. (b) Incident angle and amplification factor vs incident angle.

Fig. 11. Interfacial displacement of case B6. The dashed lines show the computational condition. The thick solid lines show the interfacial displacement of a stem. The thin solid lines show the 3rd order theoretical solution.

581

582 Fig. 12. Progress of internal solitary waves by using the interfacial displacement and velocity
583 potential around a stem. (a) case A1. (b) case A5. (c) case B1. (d) case B6.

584

585

586

587

588 **Table captions**

589

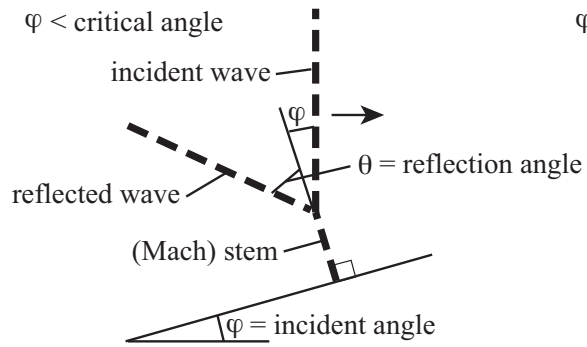
590 Table 1. Computational conditions for small and large amplitude cases.

591

592

593

Mach reflection



Regular reflection

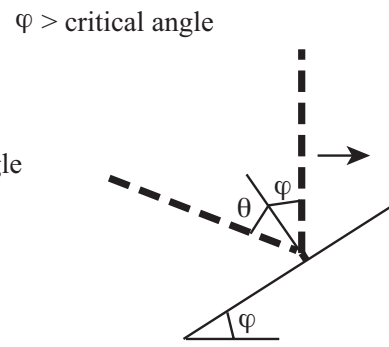
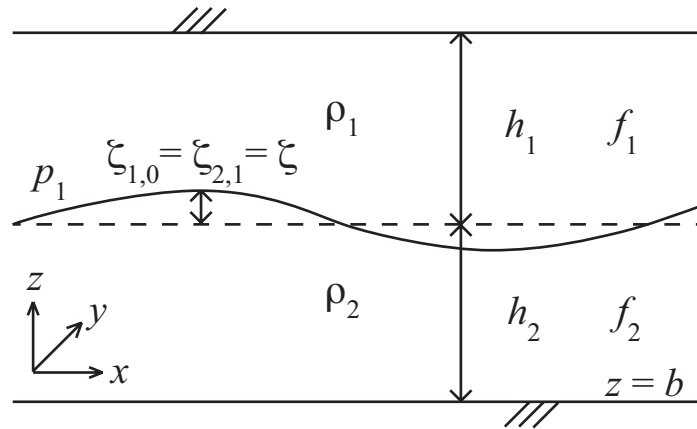


Fig. 1. Schematic horizontal plane view of a computation corresponding to the occurrence of Mach and regular reflection of a soliton with an incident angle of φ . θ indicates the reflection angle.



599

600 Fig. 2. Schematic diagram of a two-layer system. Upper and lower boundaries are considered as

601 rigid walls.

602

603

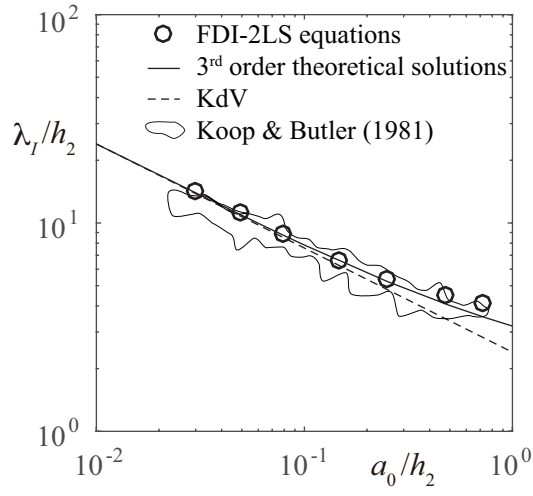


Fig. 3 Comparisons with the laboratory experiments by Koop and Butler [22]. Thin solid lines indicate the region of the experiments' plots. Dashed and thick solid lines indicate the KdV theoretical solutions and the 3rd order theoretical solutions, respectively. Circles indicate numerical computation results by using the FDI-2s equations.

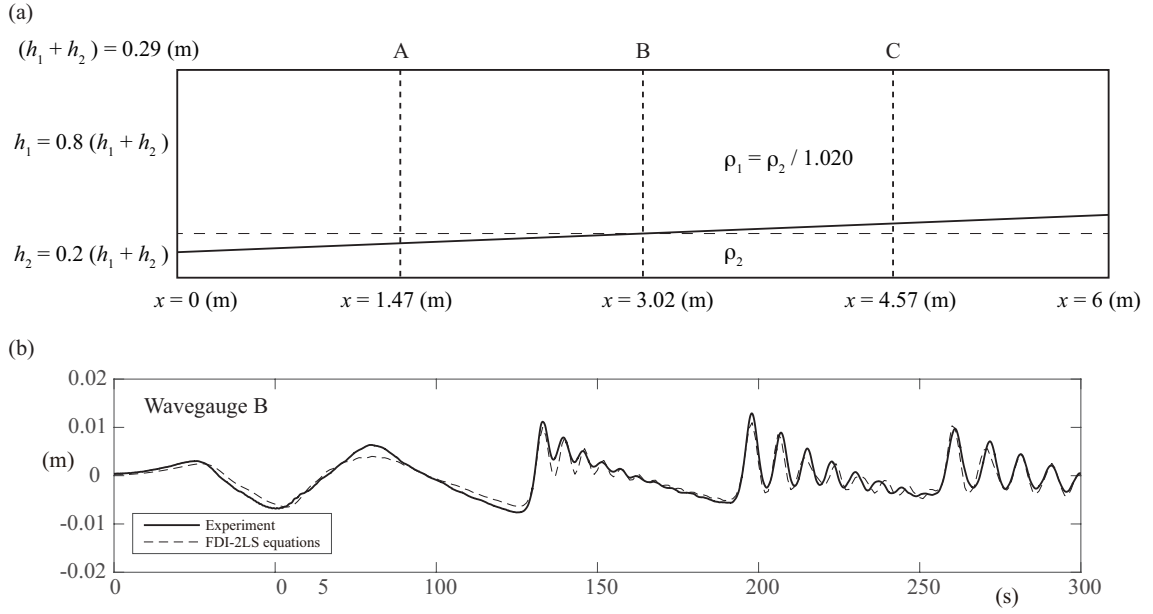
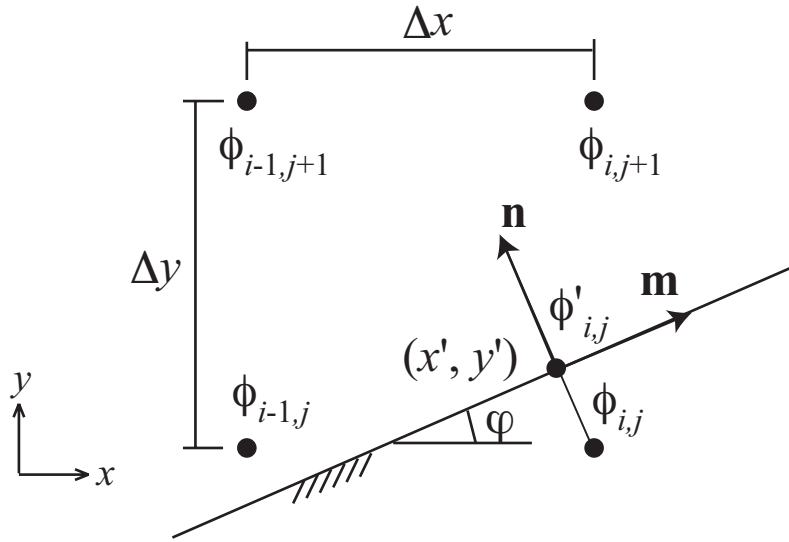


Fig. 4 Comparisons with the laboratory experiments by Horn *et al.* [17] [46] [47]. (a) Initial set up.

(b) Comparisons of interfacial displacement at the Wavegauge B between the laboratory experiments

and the FDI-2s equations.



617

618 Fig. 5. Schematic diagram for satisfying boundary conditions of momentum. Normal velocity to

619 an oblique boundary should be zero.

620

621

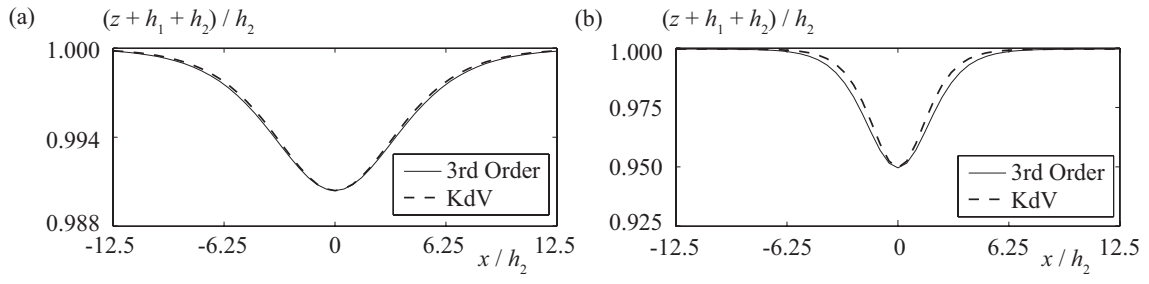


Fig. 6. Initial waves. The solid lines shows the 3rd order theoretical solution and dashed line shows the KdV solution. (a) case A. (b) case B.

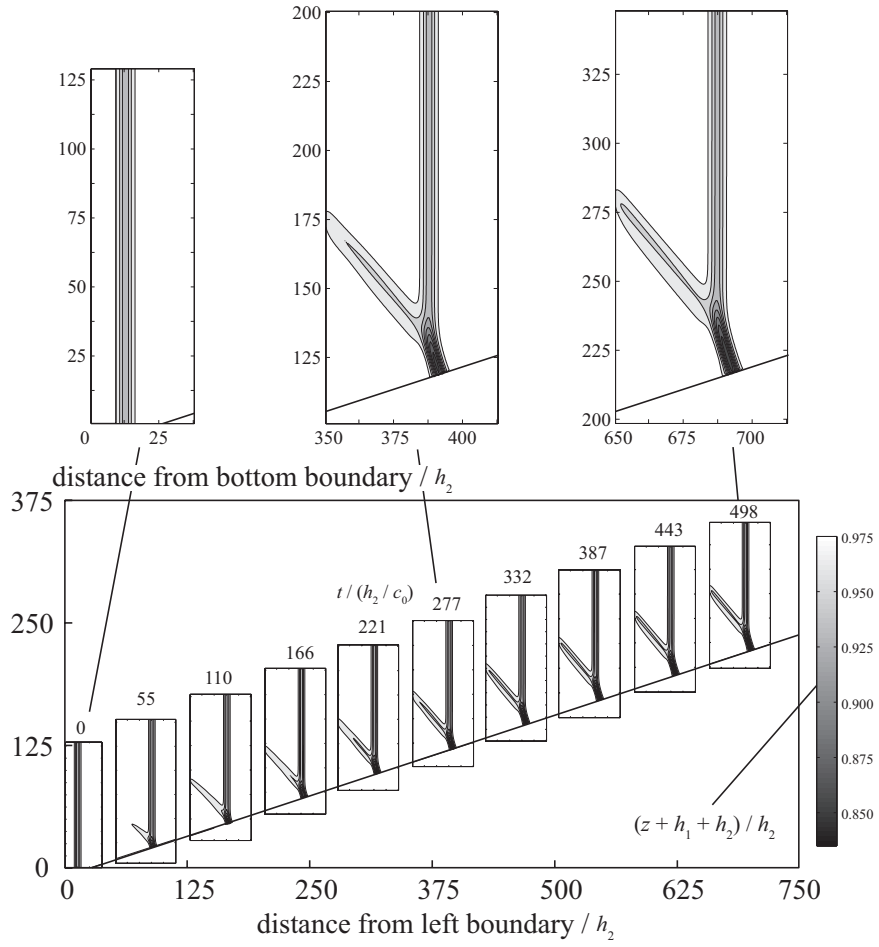
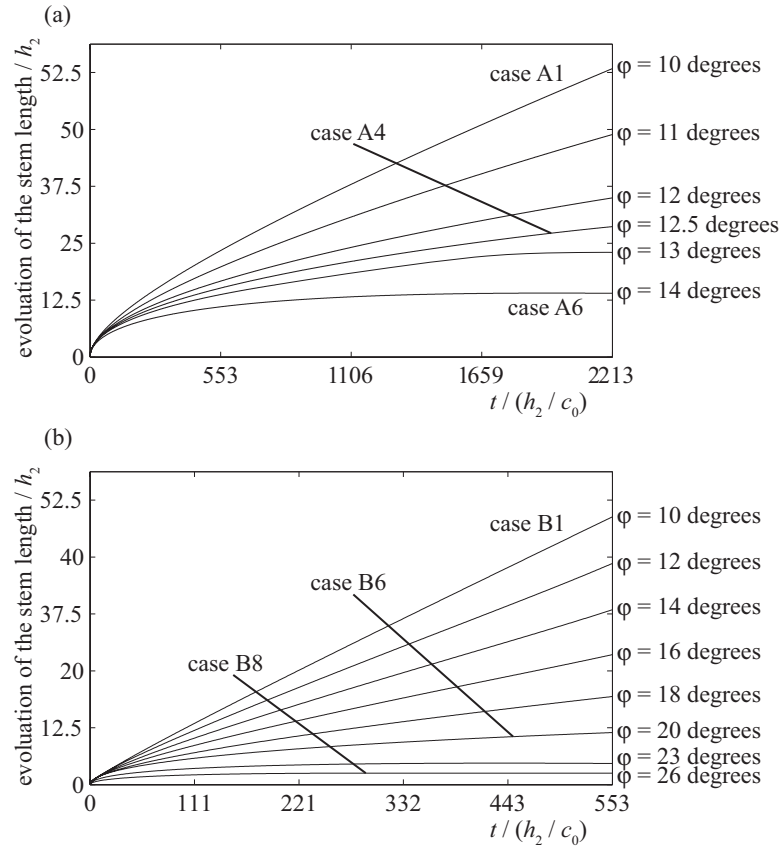


Fig. 7. Interfacial displacement of case B5. Each solid line square in the bottom figure indicates the computational region at the times indicated. Top three figures show enlarged progress of internal solitary wave at $t = 0$ s, $t = 250$ and $t = 450$ s.



633
 634 Fig. 8. Time series of the length of a stem for case A and case B. Length is normalized by the lower
 635 layer depth. (a) cases A1 to A6. (b) cases B1 to B8.

636

637

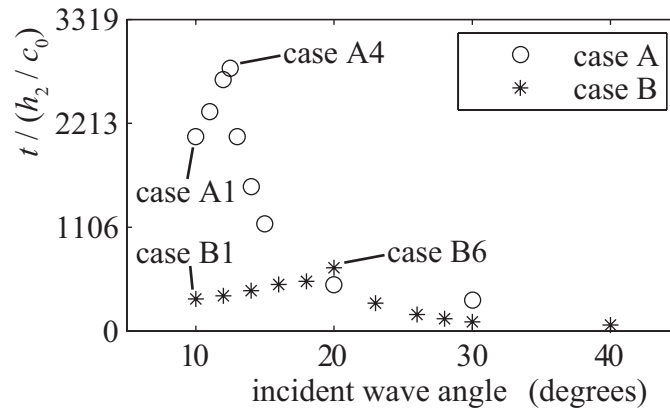
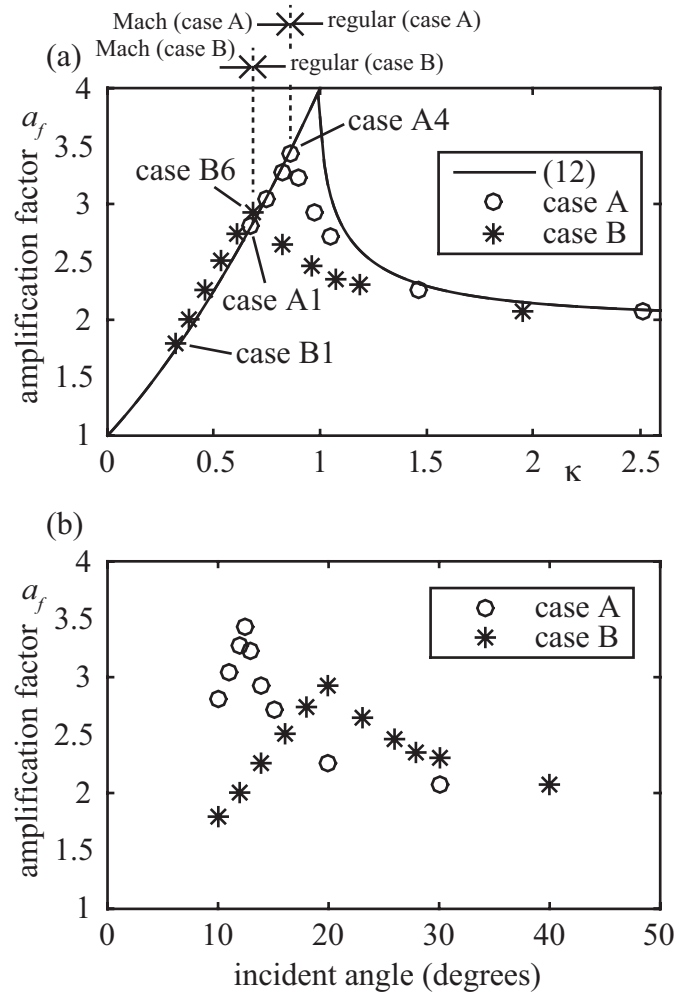


Fig. 9. Time taken to reach the maximum amplitude due to the internal soliton resonance for small amplitude case (circles) and large amplitude case (stars).



643

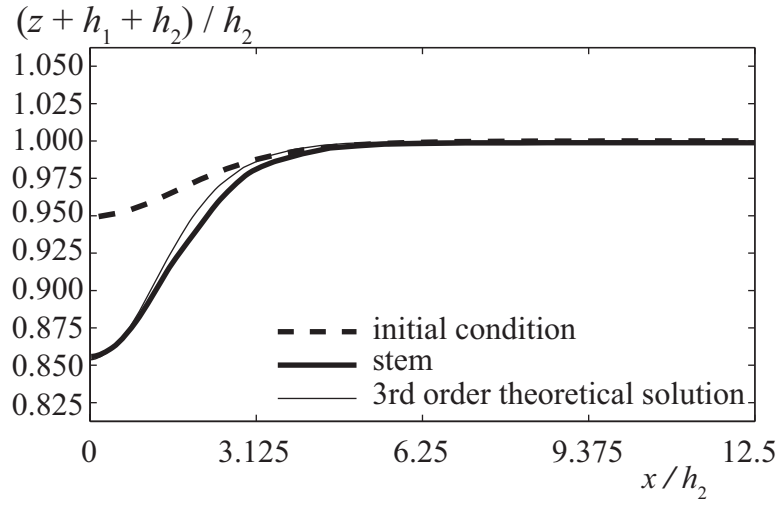
644 Fig. 10. Comparisons with (13). Circles and stars denote case A and B from the FDI-2s equations. (a)

645 Normalized amplification factor vs κ for case A and B. Solid lines show (13) [27] [30] [31]. (b) Incident

646 angle and amplification factor vs incident angle.

647

648



649

650 Fig. 11. Interfacial displacement of case B6. The dashed lines show the computational condition.

651 The thick solid lines show the interfacial displacement of a stem. The thin solid lines show the 3rd

652 order theoretical solution.

653

654

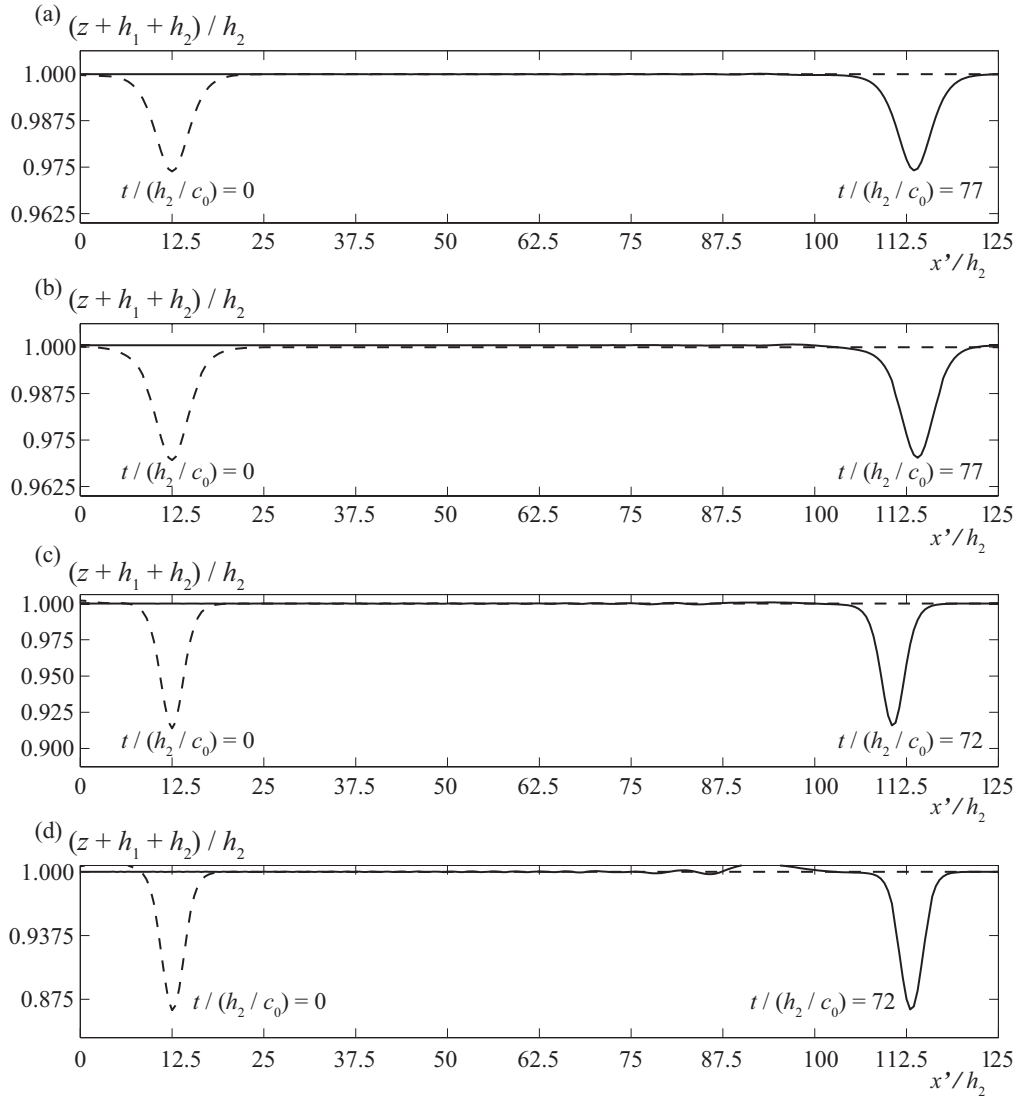


Fig. 12. Progress of internal solitary waves by using the interfacial displacement and velocity potential around a stem. (a) case A1. (b) case A5. (c) case B1. (d) case B6.

660 Table 1. Computational conditions for small and large amplitude cases.

case	a_0 / h_2	α (degree)	φ_{c_kp} (degree)	κ	amplification factor
A1	0.01	10	14.4	0.68	2.81
A2	0.01	11	14.4	0.75	3.05
A3	0.01	12	14.4	0.82	3.27
A4	0.01	12.5	14.4	0.86	3.43
A5	0.01	13	14.4	0.90	3.23
A6	0.01	14	14.4	0.97	2.92
A7	0.01	15	14.4	1.05	2.72
A8	0.01	20	14.4	1.46	2.26
A9	0.01	30	14.4	2.52	2.08
B1	0.05	10	27.7	0.32	1.79
B2	0.05	12	27.7	0.39	2.01
B3	0.05	14	27.7	0.46	2.27
B4	0.05	16	27.7	0.53	2.50
B5	0.05	18	27.7	0.61	2.74
B6	0.05	20	27.7	0.69	2.94
B7	0.05	23	27.7	0.82	2.65
B8	0.05	26	27.7	0.97	2.46
B9	0.05	28	27.7	1.07	2.35
B10	0.05	30	27.7	1.19	2.29
B11	0.05	40	27.7	1.95	2.08

661 For all cases, $h_1 = 0.2$ m, $h_2 = 0.8$ m, and $\rho_1/\rho_2 = 1.0/2.0$, respectively.

662